Nonlinear Simulation of Slab η_i Mode

Yagi, Masatoshi
Research Institute for Applied Mechanics, Kyushu University

https://doi.org/10.5109/6786342

出版情報：Reports of Research Institute for Applied Mechanics. 42 (114), pp.1-23, 1996-12. 九州大学応用力学研究所
バージョン：
権利関係：

Reports of Research Institute for Applied Mechanics
Vol. XXXXII No. 114, 1996

Nonlinear Simulation of Slab η_i Mode

By Masatoshi YAGI*

The nonlinear simulation of the slab η_i mode is performed by using the nonlinear initial value code to look for a simple but relevant simulation model for η_i mode turbulence. It is demonstrated that the two dimensional simulation of the slab η_i mode turbulence, which does not include the background profile modification, gives a good agreement with the three dimensional simulation. The thermal diffusivity is also evaluated and is compared with the mixing-length estimation. It was found that the mixing-length estimation does not give an accurate result from the viewpoint of the absolute value and the shear dependence. These tests would provide the basis to use the two-dimensional simulation for the future study of turbulence under more realistic conditions.

Key words: slab η_i mode, ion temperature driven drift wave, anomalous transport, 2D nonlinear simulation

I. Introduction

To understand the transport phenomena in high temperature plasma which is magnetically confined is one of the most important issues in the plasma physics. The evaluated thermal diffusivity based on the experimental data is much larger than that predicted by the classical theory, i. e., the binary collision of particles through Coulomb interactions. This difference is attributed to the anomalous transport which is considered to be originated from the fluctuations [1].

It is commonly accepted that the nonlinear interaction of a test wave with background fluctuations gives rise to a nonlinear damping rate $\gamma_{NL}^{(d)}$ which is written in a form of $Dk_\perp^2$, where D is an effective diffusivity and $k_\perp$ is the wave number perpendicular to the ambient magnetic field. The mode growth rate is evaluated as $\gamma=\gamma_L-\gamma_{NL}^{(d)}$($\gamma_L$ is the linear growth rate), and the stationary condition gives the estimation, $D\sim\gamma_L/k_\perp^2$[2, 3], i. e., mixing-length estimation. To confirm the validity of the mixing-length estimation, the nonlinear simulation should be necessary.

The η_i mode (ion temperature gradient driven drift wave) is one of the examples, which are often discussed by use of the mixing-length formula. It is considered to be a plausible candidate of the anomalous ion energy transport in

* Research Institute for Applied Mechanics, Kyushu University

a tokamak, and the linear stability and the nonlinear developments have been extensively studied by nonlinear simulations of drift reduced magnetohydrodynamic model[4-6](also see Ref.[7]herein references can be found). References[5, 6]reported that the numerical results are explained by the mixing-length estimations. However, a strong influence of the back ground profile modification (i. e., the local flattening of the temperature profile) on the saturation amplitude was found in these simulations. The impact of the local flattening should be analyzed in separation from the saturation mechanism of the ion nonlinearity, but there has not been a systematic study.

In this article, we report the nonlinear simulation of the slab η_i mode. The objective of this article is to look for a simple but relevant simulation model for η_i mode turbulence. The validity of the simulation (including the convergence study) is also important subject of this article.

The simulations are performed systematically employing three models; i. e., (1) the three dimensional (3D) model, (2) the two dimensional (2D) model with the local temperature flattening (abbreviated as 2D QL, the symbol QL stands for "quasi-linear") and the 2D model where the local flattening is neglected and the back-ground profile is kept constant (abbreviated as 2D NQL). It is found that the simulation result of the 2D NQL model gives a good agreement with that of the 3D one. This provides a rapid method for the future parameter survey. Some effort to obtain the fitting formula of χ is also reported. We confirmed that the 2D QL model overestimates the stabilizing influence of the local flattening, i. e., underestimates χ. The mixing-length-like estimate is found to overestimate χ.

This paper is organized as follows. The model equation is explained in Sec. II and the linear instability is revised in Sec. III. The result of nonlinear simulation is discussed in Sec. IV. The discussion and conclusion are given in Sec. V.

II. Model Equation

We first briefly review the model equations for η_i mode. We start from the electron and ion momentum equations parallel to the ambient magnetic field:

$$n_0 m_e \frac{dv_{\parallel e}}{dt} = -\nabla_\parallel p_e + en_0\left(\frac{\partial A}{\partial t} + \nabla_\parallel \phi\right) + en_0\eta j, \tag{1}$$

$$n_0 m_i \frac{dv_{\parallel i}}{dt} = -\nabla_\parallel p_i - en_0\left(\frac{\partial A}{\partial t} + \nabla_\parallel \phi\right) - en_0\eta j, \tag{2}$$

where $v_{\parallel e}$ and $v_{\parallel i}$ are electron and ion parallel velocity, p_e and p_i, electron and ion pressure, $j = en_0(v_{\parallel i} - v_{\parallel e})$ represents the parallel current, ϕ, the electrostatic potential, A, the electromagnetic potential, respectively. If we take the electrostatic limit, then we have

$$j = \frac{-(e^2 n_0/m_e) ik_\parallel}{-iw + e^2 n_0 \eta/m_e}\left(\phi - \frac{P_e}{en_0}\right), \tag{3}$$

and

$$v_{\parallel i}=\frac{k_\parallel}{n_0 m_i \omega}(p_e+p_i), \tag{4}$$

where the terms with $O(m_e/m_i)$ are neglected in Eqs. (3) and (4). From Eqs. (3) and (4), we can see if the electron response is adiabatic i. e., $n=en_0\phi/T_{e0}$ then the approximation relation $j=0$ holds (where $T_e=T_{e0}$ is assumed). On the other hand, if the electron response is far from the adiabatic relation, then the ion parallel velocity is negligible compared to j since $j\sim-(m_i/m_e)en_0v_{\parallel i}$. In the former limit, the ion continuity equation and the adiabatic electron response describe the ion temperature gradient driven drift mode turbulence (i. e., η_i mode turbulence). In the latter limit we can consider the dissipative (drift) interchange/ballooning mode turbulence discussed in Ref [8]. Generally, the turbulence may have both characteristics, which depends on the deviation from the adiabatic relation $n=en_0/T_{e0}(1+i\delta)\phi$(the η_i mode limit, $\delta\to0$, and non ideal interchange/ballooning mode limit, $\delta\gg m_e/m_i$). However, the objective of this article is not to find the most proper equation of tokamaks but to report the appropriate simulation model through nonlinear simulation. We focus to the former limit (the η_i mode turbulence).

II-A. Reduced Model Equation for η_i Mode Turbulence

Now, we consider slab η_i mode turbulence[4, 5, 9]. Basic equations are consist of the ion continuity equation, the ion parallel momentum equation, and the ion pressure balance equation [5, 10]. Here the ion continuity equation is obtained by assuming that the electron obeys the Boltzmann relation $\tilde{n}_e=en_0\phi/T_{e0}$ and using the quasi-neutrality condition $\tilde{n}_i=\tilde{n}_e$.

$$(1-\nabla_\perp^2)\frac{\partial\phi}{\partial t}=-(1+K\nabla_\perp^2)\frac{\partial\phi}{\partial y}-\nabla_\parallel v+[\phi,\ \nabla_\perp^2\phi]-\mu_{\perp c}\nabla_\perp^4\phi, \tag{5}$$

$$\frac{\partial v}{\partial t}=-\nabla_\parallel(\phi+p)-[\phi,\ v]+\mu_{\perp c}\nabla_\perp^2 v+\mu_{\parallel c}\nabla_\parallel^2 v, \tag{6}$$

$$\frac{\partial p}{\partial t}=-K\frac{\partial\phi}{\partial y}-\Gamma\nabla_\parallel v-[\phi,\ p]+\chi_{\perp c}\nabla_\perp^2 p+\chi_{\parallel c}\nabla_\parallel^2 p. \tag{7}$$

Poission's bracket denoting the $\mathbf{E}\times\mathbf{B}$ nonlinearity is defined as $[\phi,\ A]\equiv\partial\phi/\partial x\partial A/\partial y-\partial\phi/\partial y\partial A/\partial x$. For the above equations, the following normalization is employed : $(c_s/L_n)t\to t$, $r/\rho_s\to r$, $(eL_n/T_e\rho_s)\phi\to\phi$, $(L_n/c_s\rho_s)v_{\parallel i}\to v$, $(\tau L_n/\rho_s p_{e0})p_i\to p$, $(L_n/n_0m_i\rho_s^2c_s)\mu\to\mu$, $(L_n/\rho_s^2c_s)\chi\to\chi$, $L_n^{-1}=-d\ln n_0/dr$, $c_s=\sqrt{T_{e0}/m_i}$, $\rho_s=c_s/\Omega_i$, $\Omega_i=eB/m_i$, $\tau=T_{e0}/T_{i0}$, $\Gamma=5/(3\tau)$, $K=(1+\eta_i)/\tau$, $\eta_i=L_n/L_{Ti}$, $L_{Ti}^{-1}=-d\ln T_{i0}/dr$, $\nabla_\parallel=\partial/\partial z+Sx\partial/\partial y$, $S=L_n/L_s$, $L_s^{-1}=(r/Rq^2)dq/dr$, $\nabla_\perp^2=\partial^2/\partial x^2+\partial^2/\partial y^2$ where $x=r-r_0$, r_0 represents the location of the rational surface. $\mu_{\perp,\parallel c}$ and $\chi_{\perp,\parallel c}$ are the collisional viscosity and thermal conductivity, respectively. The coordinates (x, y, z) are taken such that x is the direction of density and temperature gradients, z in that of the ambient magnetic field at x=0, and y in that of perpendicular to x and z, respectively, and correspond to the cylindrical

coordinates $(r-r_0,\ \theta,\ \zeta-q(r_0)\theta)$. The parameter K represents the ion pressure gradient, i. e., the driving force of the turbulence. The Boussinesq approximation is used to derive these equations [11].

II-B. Eenegy Conservation Relation and Thermal Diffusivity for η_i Mode Turbulence

The energy evolution of these equations is written as follows;

$$\frac{dE_T}{dt}=\frac{K\tau}{\Gamma}\langle\phi^*\frac{\partial p}{\partial y}\rangle-K\langle p^*\nabla_\perp{}^2\frac{\partial\phi}{\partial y}\rangle-\mu_{\perp c}\langle|\nabla_\perp{}^2\phi|^2\rangle$$
$$-\mu_{\perp c}\langle|\nabla_\perp v|^2\rangle-\mu_{\parallel c}\langle\nabla_\parallel v|^2\rangle-\chi_{\perp c}\langle\nabla_\perp p|^2\rangle-\chi_{\parallel c}\langle|\nabla_\perp p|^2\rangle, \tag{8}$$

where

$$E_T=E_\phi+E_{\nabla\perp\phi}+E_v+E_p, \tag{9}$$

with $E_\phi=\frac{1}{2}\langle|\phi|^2\rangle$, $E_{\nabla\perp\phi}=\frac{1}{2}\langle|\nabla_\perp\phi|^2\rangle$, $E_v=\frac{1}{2}\langle|v|^2\rangle$, $E_p=\frac{1}{2}\frac{\tau}{\Gamma}\langle|p|^2\rangle$. E_ϕ denotes the perturbed internal energy of electrons, $|\tilde{p}_e|^2/2$. (It should be noted that the Boltzmann relation for electrons with $\tilde{T}_e=0$ is assumed in the model of the η_i mode.) $E_{\nabla\perp\phi}$ corresponds to the electric field energy (and is almost equal to the kinetic energy of perpendicular ion motion), E_v to the kinetic energy of the ion parallel motion, and E_p to the ion internal energy. $\langle\rangle$ is defined as

$$\langle f\rangle=\frac{1}{L_xL_yL_z}\int_{-L_x/2}^{L_x/2}dx\int_0^{L_y}dy\int_0^{L_z}dzf(x,\ y,\ z), \tag{10}$$

where L_x, L_y and L_z are the system size of the simulation in the x, y and z directions, respectively.

Nothing the relation, $\chi_i=\overline{\langle\tilde{p}_i\cdot\tilde{v}_{ir}\rangle}/(-p'_{i0})$, we obtain the normalized ion thermal diffusivity

$$\chi_i=-\frac{1}{K}\frac{L_x}{\Delta_x}\langle p^*\frac{\partial\phi}{\partial y}\rangle, \tag{11}$$

where

$$\overline{g(t)}=\lim_{T\to\infty}\frac{1}{T}\int_0^T g(t)dt. \tag{12}$$

For the 3D case $\Delta_x=L_x$. For the 2D case, we choose

$$\Delta_x=\int_0^{L_x}\Theta(f(x)-0.1f_{max})dx, \tag{13}$$

where Θ is the Heaviside step function and f_{max} is the maximum value of $|f(x)|$ on $|x|<L_x/2$. For 2D case, the size of the mode width Δ_x is used as normalization factor in Eq.(11) to get rid of the system size effect on the averaged value of χ_i since the mode is localized near rational surface in the 2D model. The definition of Δ_x is in accordance with those in Ref. [5]. The error bar is

estimated during steady state phase,

$$(\Delta\chi_i)^2=\overline{(\chi_i(t)-\chi_i)^2}. \tag{14}$$

The power spectrum of $W_\phi(k_y,k_z)$, $W_{\nabla_\perp\phi}(k_y, k_z)$, $W_v(k_y,k_z)$, $W_p(k_y, k_z)$ are defined as

$$W_\phi(k_y, k_z)=\frac{1}{L_x}\int_0^{L_x} dx\frac{1}{2}|\phi(x, k_y, k_z)|^2,\ W_{\nabla_\perp\phi}(k_y, k_z)=\frac{1}{L_x}\int_0^{L_x} dx\frac{1}{2}|\nabla_\perp\phi(x, k_y, k_z)|^2,\ W_v(k_y, k_z)=\frac{1}{L_x}\int_0^{L_x} dx\frac{1}{2}|v(x, k_y, k_z)|^2,\ W_p(k_y, k_z)=\frac{1}{L_x}\int_0^{L_x} dx\frac{1}{2}|p(x, k_y, k_z)|^2, \tag{15}$$

and $W_T(k_y, k_z)=W_\phi(k_y, k_z)+W_{\nabla_\perp\phi}(k_y, k_z)+W_v(k_y, k_z)+W_p(k_y, k_z)$. We also define the radial profiles of the thermal flux as

$$Q(x)=-\frac{1}{L_yL_z}\int_0^{L_y} dy\int_0^{L_z} dz p^*\frac{\partial\phi}{\partial y}. \tag{16}$$

III. Linear Stability Analysis

First of all, we revise the linear stability of slab η_i mode[4, 5, 9]. Equations (5)-(7) contain the linear instability of the slab η_i mode. In the limit of $\mu_{\perp,\parallel c}=\Gamma=0$, the eigenfrequency ω is given as

$$\frac{\omega}{k_y}=\frac{1-Kk_y^2-i|S|(2l+1)\pm\sqrt{\{1-2Kk_y-i|S|(2l+1)\}^2-i4K|S|(2l+1)(1+k_y^2)}}{2(1+k_y^2)} \tag{17}$$

where l is the radial node number, ω and k_y are normalized by c_s/L_n and ρ_s, reapectively. For the case with $l=0$, $k_y\ll 1$ and $S\gg 1$, the maximum growth rate is given by $\gamma\simeq K^{1/2}S^{1/2}$ with $k_y^2\simeq 1/K$, and in the another limit satisfying $|1-Kk_y^2|>2K^{1/2}S^{1/2}$, and $|Kk_y^2|\ll 1$, we have $\gamma\simeq KS$. When $\mu_{\perp,\parallel c}$, $\chi_{\perp,\parallel c}$, Γ are finite, both the longer wavelength modes and the shorter wavelength modes are stabilized. The effect of finite $\chi_{\perp,\parallel c}$ and Γ on the growth rate of the slab η_i mode is discussed in Ref.[5].

Figure 1 shows the dependence of the growth rate on the wave number. As a typical example of the weak shear limit, we choose the following parameters: $K=2$, $S=0.1$, $\Gamma=2$, $\mu_{\perp c}=\chi_{\perp c}=0.01$, $\mu_{\parallel c}=\chi_{\parallel c}=1.0$. 6 cases with the different radial node number ($l=0-5$) are plotted. For these parameters, the maximum growth rate is given by $\gamma_{max}=0.148$ with $k_y=0.8$ for $l=1$ mode. The hatched region shows the mode with $l=1$ is dominant, on the other hand, for $k_y>1.6$, the mode with $l=2$ is dominant. The mode is stabilized for $k_y>2.0$.

Figure 2 shows the dependence of the growth rate on the ion pressure gradient. The parameter $k_y=0.8$ is used in this calculation. Other parameters are the same as those in Fig. 1. The dominant radial mode number is $l=1$ for $K<3.5$ and is $l=2$ for $K>3.5$. For $K<K_c\sim 0.7$, all the modes become linearly stable.

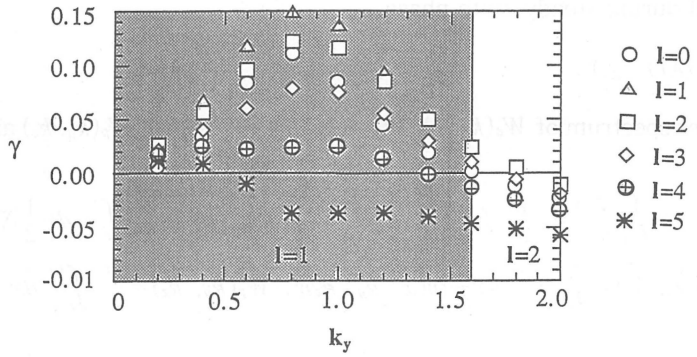

Fig. 1 The linear growth rate of slab η_i mode versus k_y. Parameters are given by $K=2$, $S=0.1$, $\Gamma=2$, $\mu_{\perp c}=\chi_{\perp c}=0.01$, $\mu_{\parallel c}=\chi_{\parallel c}=1.0$.

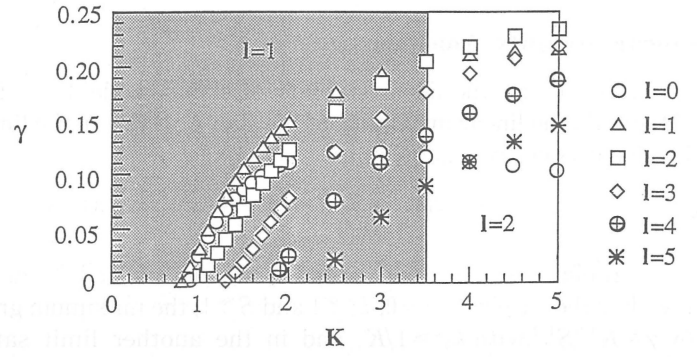

Fig. 2 The linear growth rate of slab η_i mode versus K. Parameters are given by $k_y=0.8$, $S=0.1$, $\Gamma=2$, $\mu_{\perp c}=\chi_{\perp c}=0.01$, $\mu_{\parallel c}=\chi_{\parallel c}=1.0$.

Figure 3 shows the dependence of the growth rate on the parallel thermal diffusivity. Here the relation $\mu_{\parallel c}=\chi_{\parallel c}$ is assumed. Other parameters are the same as those in Fig. 2. It is found that the dominant mode is the one with $l=2$ for $\chi_{\parallel c}\leq 0.1$, with $l=1$ for $0.1\leq\chi_{\parallel c}\leq 2$, and with $l=0$ for $2\leq\chi_{\parallel c}\leq 100$. All modes are completely stabilized for $100\leq\chi_{\parallel c}$.

Figure 4 shows the linear eigenfunction of the η_i mode with the maximum growth rate at $k_y=0.8$. Parameters are given by $K=2$, $S=0.1$, $\Gamma=2$, $\mu_{\perp c}=\chi_{\perp c}=0.01$, $\mu_{\parallel c}=\chi_{\parallel c}=0.1$. The thick curve shows the real part of ϕ and the dashed curve shows the imaginary part of ϕ. The mode is localized near the mode rational surface $x\sim 40$. This is a typical example of the drift wave eigenfunction.

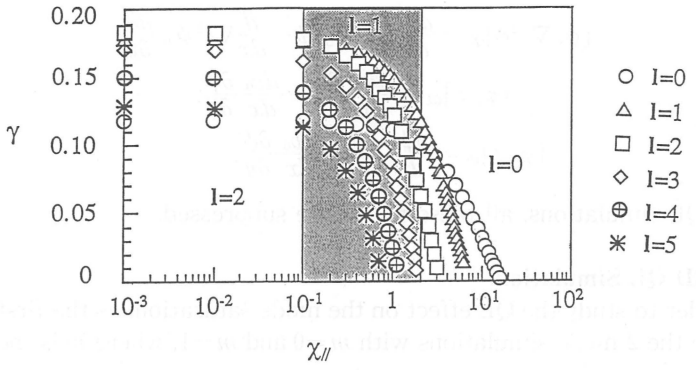

Fig. 3 The linear growth rate of slab η_i mode versus $\chi_{\parallel}$. Parameters are given by $\mu_{\parallel c} = \chi_{\parallel c}$, $k_y = 0.8$, $K = 2$, $S = 0.1$, $\Gamma = 2$, $\mu_{\perp c} = \chi_{\perp c} = 0.01$.

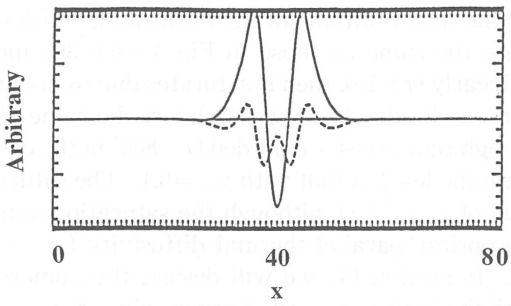

Fig. 4 The linear eigenfunction of η_i mode with maximum growth rate at $k_y = 0.8$. Parameters are given by $K = 2$, $S = 0.1$, $\Gamma = 2$, $\mu_{\perp c} = \chi_{\perp c} = 0.01$, $\mu_{\parallel c} = \chi_{\parallel c} = 0.1$.

IV. Nonlinear Simulation

Next, we discuss the nonlinear simulation of slab η_i mode. Equations (5)-(7) are solved by using the predictor-corrector method with the finite difference for the x space and with the fourier transform for the y space. In these simulations, we have performed two types of simulations, that is, the case where the background profile modification is taken into account, and the case where it is not kept. In QL simulations, we keep the following QL terms in the equations,

$$[\phi, \nabla_\perp^2\phi]_{QL}=\frac{d\phi_0}{dx}\frac{\partial}{\partial y}\nabla_\perp^2\phi-\frac{d}{dx}\nabla_\perp^2\phi_0\frac{\partial\phi}{\partial y},$$
$$[\phi, v]_{QL}=\frac{d\phi_0}{dx}\frac{\partial v}{\partial y}-\frac{dv_0}{dx}\frac{\partial\phi}{\partial y},$$
$$[\phi, p]_{QL}=\frac{d\phi_0}{dx}\frac{\partial p}{\partial y}-\frac{dp_0}{dx}\frac{\partial\phi}{\partial y}. \tag{18}$$

and in NQL simulations, all these terms are suppressed.

IV-A. 2D QL Simulation

In order to study the QL effect on the mode saturation, as the first step, we have done the 2 mode simulations with $m=0$ and $m=1$, where m is the poloidal mode number.

Table 1 shows the dependence of the saturation amplitude of total energy on the mesh number. Parameters are the same as those in Fig. 4. We change mesh number from 200 to 500. For the two-modes case, we conclude that it is enough to take 200 mesh.

Figure 5 shows the time evolution of the total energy with various values of $\chi_{\parallel c}$. Parameters are the same as those in Fig. 4 with 300 mesh. Firstly the energy is growing linearly ($t\leq 10$), then it saturates due to nonlinear effects ($t\geq 10$). The saturation amplitude of energy is almost the same level in the range $\chi_{\parallel c}\sim 0.1-1$, but enough time steps are needed ($t\geq 800$) in the cases with $\chi_{\parallel c}=0.5$ and $\chi_{\parallel c}=1.0$ to attain the level of that with $\chi_{\parallel c}=0.1$. The saturation is observed even for small value of $\chi_{\parallel c}(\leq 0.1)$, although the saturation amplitude is larger. Practically, an appropriate parallel thermal diffusivity ($\chi_{\parallel c}\sim 1$) is needed for numerical stability. In section IV, we will discuss the numerical convergence which is related with the limit of $\chi_{\parallel c}\to 0$. Larger value of $\chi_{\parallel c}(\geq 1)$ gives smaller

Table 1 The dependence of the saturation amplitude of total energy on mesh number. Parameters are given by $k_y=0.8$, $K=2$, $S=0.1$, $\Gamma=2$, $\mu_{\perp c}=\chi_{\perp c}=0.01$, $\mu_{\parallel c}=\chi_{\parallel c}=0.1$.

time	200 mesh	300 mesh	400 mesh	500 mesh
100	0.46250	0.46000	0.46000	0.46000
200	0.35800	0.35670	0.35500	0.35600
300	0.32000	0.31830	0.31750	0.31800
400	0.31600	0.31500	0.31500	0.31400
500	0.33500	0.33670	0.33750	0.33600
600	0.37900	0.38330	0.38250	0.38400

saturation amplitude of energy which corresponds to linear stabilization of modes (also see Fig. 3).

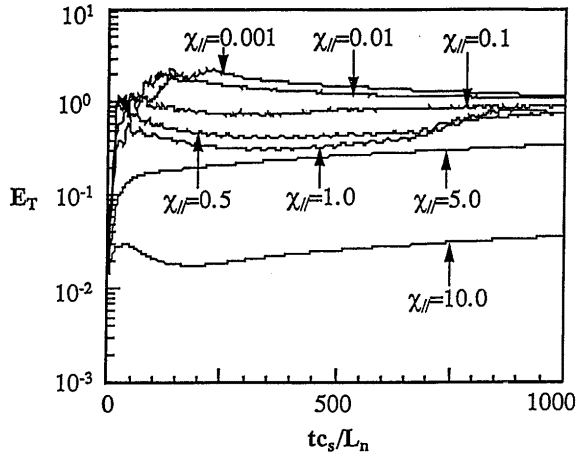

Fig. 5 The time evolution of the total energy in 2D QL calculations with various values of $\chi_{\parallel c}$. Seven cases, with $\chi_{\parallel c} = 0.001, 0.01, 0.1, 0.5, 1.0, 5.0, 10.0$ are plotted. Other parameters are the same as those in Fig. 4.

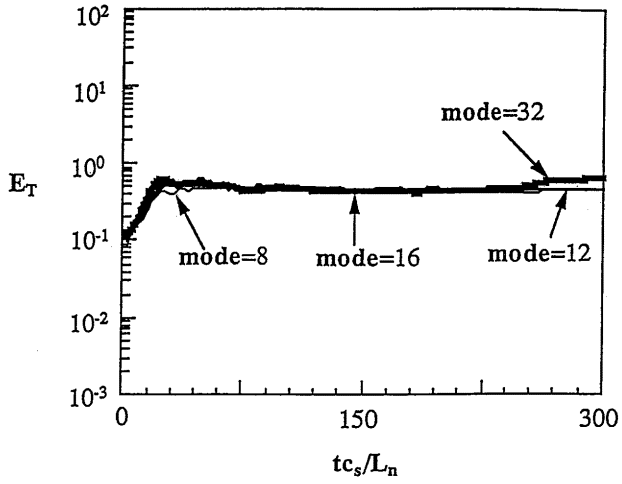

Fig. 6 The time evolution of energy in 2D QL calulation and it's mode number dependence. Parameters are $k_{y0} = 0.2$, $K = 2$, $S = 0.1$, $\Gamma = 2$, $\mu_{\perp c} = \chi_{\perp c} = 0.01$, and $\mu_{\parallel c} = \chi_{\parallel c} = 1.0$. Four cases with $M = 8, 12, 16, 32$ are plotted.

Next, we discuss multi-modes simulation with QL effects. Figure 6 shows time evolutions of energy in 2D QL simulations and their mode number dependence. Parameters are $L_x=80$ with 300 mesh, $k_{y0}=0.2$ (which corresponds to the system size of y, i. e. $L_y=2\pi/k_{y0}$), and $\mu_{\parallel c}=\chi_{\parallel c}=1.0$. Other parameters are the same as those in Fig. 4. Four cases with mode number, M=8, 12, 16, and 32 are plotted. We found that the saturation amplitude of energy weakly depends on mode number in 2D QL simulations.

Figure 7 shows time averaged fluctuation spectra in the case with M=12 shown in Fig. 6. Time averge is taken from t=100 to 300. W_ϕ, $W_{\nabla_\perp\phi}$, W_v, W_p are plotted. The energy cascade is observed in these spectra and the energy

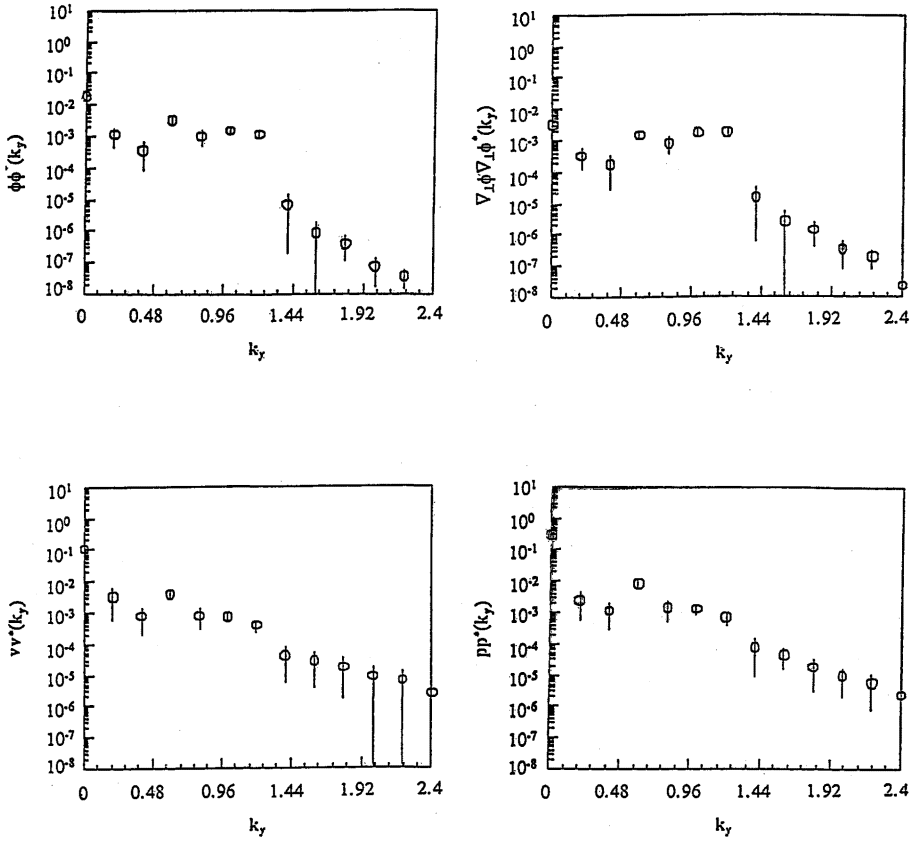

Fig. 7 The time averaged fluctuation spectrum for the case with $M = 12$ in Fig. 6. Time average is taken from $t = 100$ to 300. $W_\phi(k_y)$, $W_{\nabla_\perp\phi}(k_y)$, $W_v(k_y)$, $W_p(k_y)$ are plotted.

tends to concentrate at m=0 mode in this case.

IV-B. 2D NQL Simulation

In this section, we investigate 2D NQL model. The main subject is to identify how the background profile modification affects the saturation ampli-

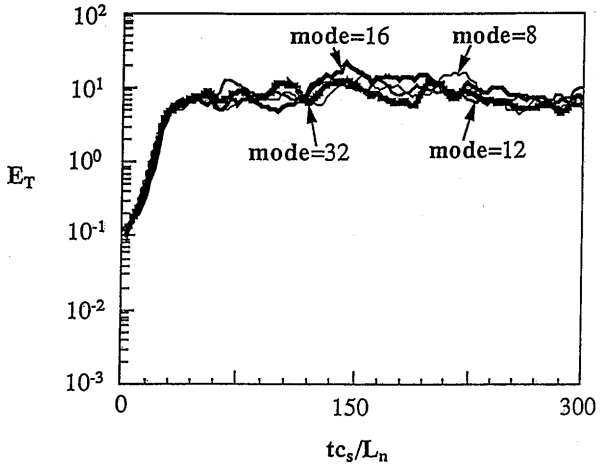

Fig. 8 The time evolution of energy in 2D NQL calculations with fixed system size ($k_{y0} = 0.2$). Parameters are the same as those in Fig. 6. Four cases with $M = 8, 12, 16, 32$ are plotted.

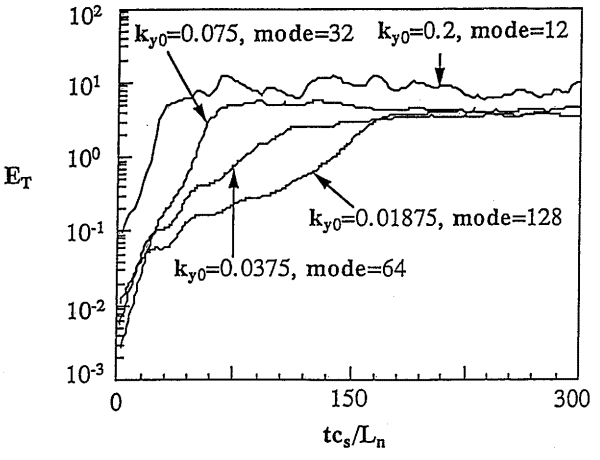

Fig. 9 The time evolution of energy in 2D NQL calculations with fixed mesh size ($k_{ymax} = 2.4$). Other parameters are the same as those in Fig. 6. Four cases with $M = 12, 32, 64, 128$ are plotted.

tude of the energy.

Figure 8 shows time evolution of energy in 2D NQL simulations with the minimum wave number fixed at $k_{y0}=0.2$, i. e., with fixed system size. Four cases with M=8, 12, 16, and 32, where M is the number of the poloidal mode kept in the simulation, are plotted. Parameters are the same as those in Fig. 6 except QL effect. We found that the saturation amplitudes of energy are almost the same level among four mode numbers and are about 10 times larger than QL one in 2D model. Compared to QL case, the energy tends to be oscillatory.

Figure 9 shows time evolution of energy in 2D NQL simulations with the maximum wave number fixed at $k_{ymax}=2.4$, i. e., with fixed mesh size. Four cases with $M=12$, 32, 64, 128 are plotted. Parameters are the same as those in Fig. 8. In the case with M=12, the saturation amplitude of energy is higher than

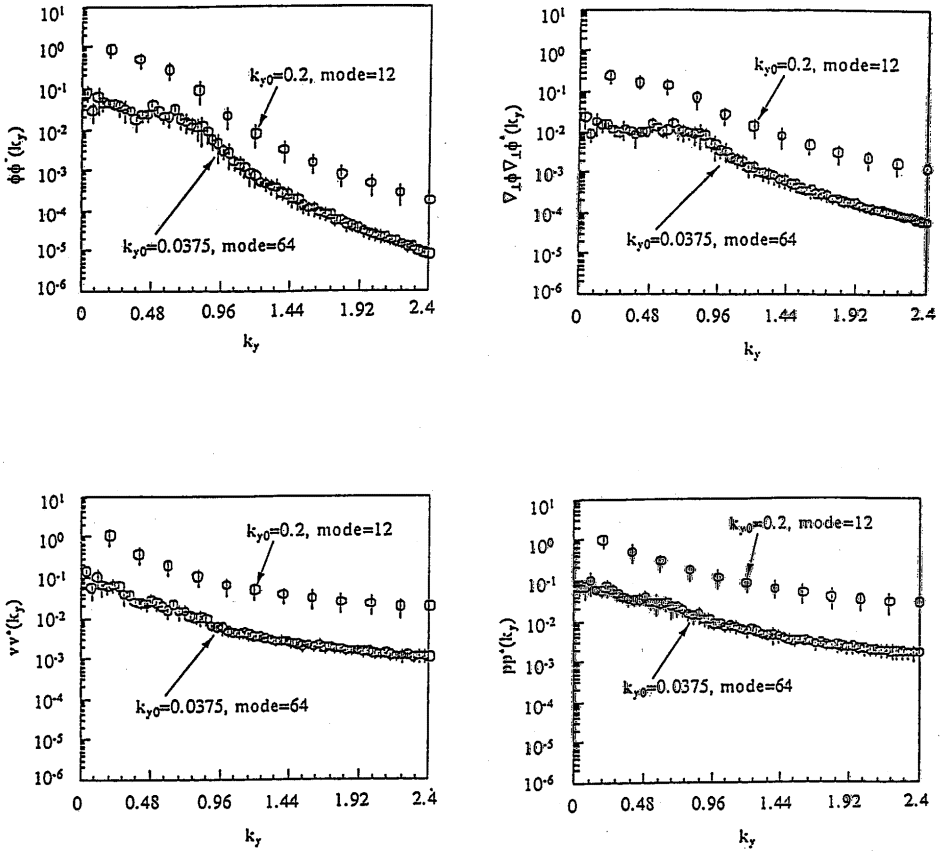

Fig. 10 The time averaged power spactrum ($t=100-300$) in Fig. 9. $W_\phi(k_y)$, $W_{\nabla_\perp\phi}(k_y)$, $W_v(k_y)$, $W_p(k_y)$ are plotted in cases with $M=12$, and $M=64$.

those in other cases. For the simulations with mode number larger than 32, the amplitude is almost the same level. This indicate that the number of mode, $M \geq 64$ is large enough to recover the convergence of saturation level. Rutherford regime [12] appears under the condition if the mode number is taken large enough (≥ 64) and the maximum wave number is fixed. This slow growth of the energy may be related that the equipartition of energy to the long wave length mode needs longer time.

Figure 10 shows time averaged power spectrum (t=100-300) for the case with M=64 shown in Fig. 9. The case with M=12 is also plotted for comparison. The shapes of energy spectrum are almost similar for both cases but the absolute value in the case of M=12 is about 10 times larger than that with M=64. The concentration of the energy to $k_y=0$ does not occur in 2D NQL simulations.

Figure 11 shows the time evolution of power spectrum of $E_T(k_y)$ in the case with M=12 shown in Fig. 9. Both normal and inverse cascades are observed at $t=60$. Strong inverse cascade occurs at t=80 and finally the spectrum reaches the steady at $t=100$. The energy tends to be consentrate on the longest wave number.

Figure 12 shows the spectral intensity of the potential for the case of M=64 shown in Fig. 9. Sampling time is taken as t=120-910. Four cases with $x=0$, and with $k_y=0.075$, 0.3, 0.45, and 0.6 are shown. The negative sign on ω axis corresponds to the ion diamagnetic direction in these figures. The peaked frequency is given by $\omega_{peak}=8.18\times10^{-3}$ for $k_y=0.075$, $\omega_{peak}=-0.188$ for $k_y=0.3$, $\omega_{peak}=-0.147$, for $k_y=0.45$ and $\omega_{peak}=2.45\times10^{-2}$ for $k_y=0.6$, respectively. In the region of the long wave length ($k_y\leq0.45$), the dominant frequency is in the

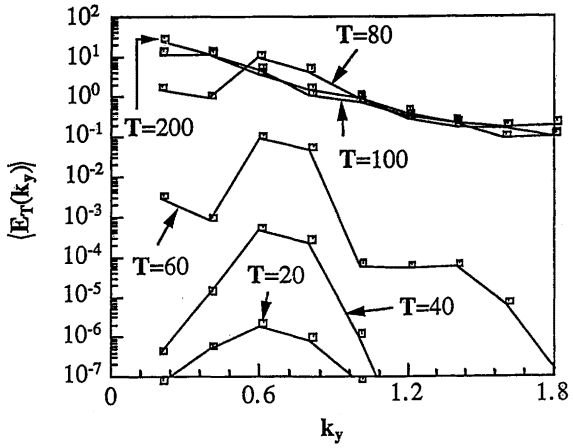

Fig. 11 The time evolution of power spectrum of $W_T(k_y)$ for the case with $M = 12$ in Fig. 9.

ion diamagnetic direction. However it is difficult to verify the linear dispersion relation, since the relation $\Delta\omega/\omega \sim O(1)$ shows the strong turbulence state.

IV-C. 3D Simulation

The results in previous subsection shows that in 2D simulations, the saturation amplitude strongly depends on the model with/without background profile modification effect. Here we perform the 3D simulations and compare the results with 2D simulations with/without QL effect.

Figure 13 shows the time evolutions of the energy in 3D QL (3 dimensional

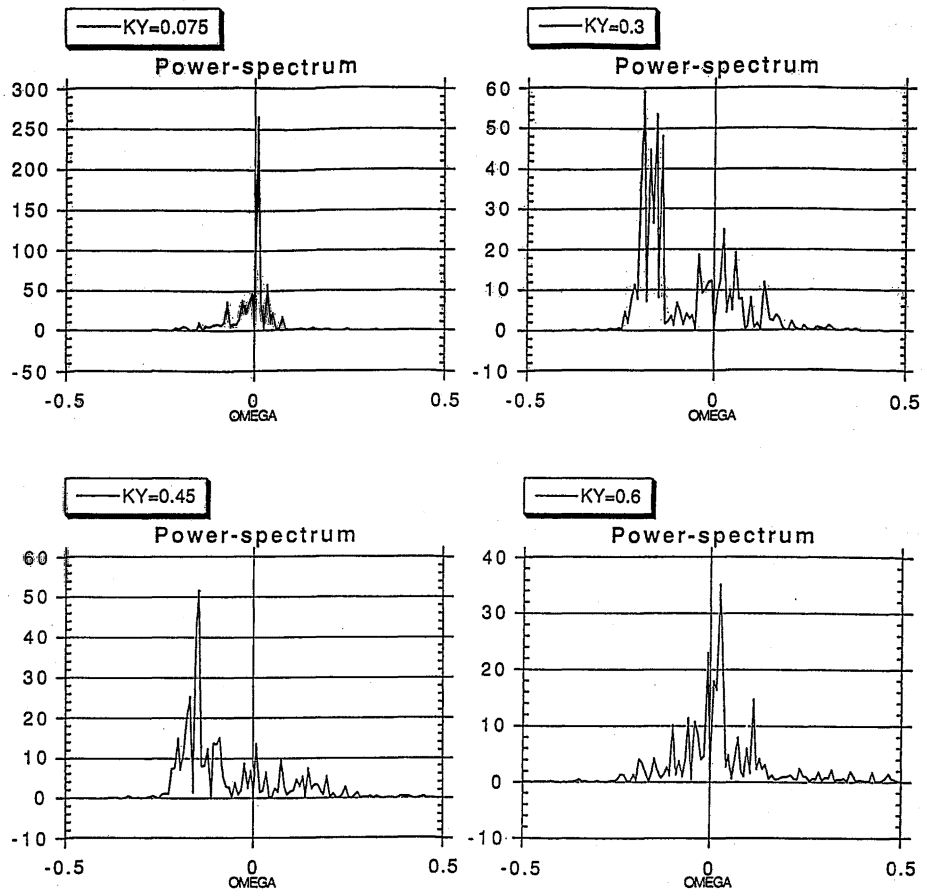

Fig. 12 The spectral intensity of the potential in the case with $M = 64$ in Fig. 9. Four cases with $k_y = 0.075, 0.3, 0.45, 0.6$ at the fixed point $x = 0$ are plotted. The minus sign on ω axis corresponds to the ion diamagnetic direction.

quasi-linear) and 3D NQL (non quasi-linear) calculations. Selection of modes are as follows: $L_x=80$ with 200 mesh, $L_y=10\pi$, $L_z=7.5\pi$, $k_{y0}=0.2$, $k_{z0}=0.267$, where $k_{y0}=2\pi/L_y$, and $k_{z0}=2\pi/L_z$. Mode numbers in the k_y space are $M=10$ and those in the k_z space are $N=13$. The modes of $k_y=mk_{y0}(0\leq m\leq 9)$, $k_z=nk_{z0}(-6\leq n\leq 6)$ are kept. Parameters are: $S=0.1$, $K=3.0$, $\Gamma=2.0$, $\mu_{\perp c}=\chi_{\perp c}=0.1$, $\mu_{\parallel c}=\chi_{\parallel c}=1.0$. For comparison, we also plot the results of 2D NQL simulation, in which modes are selected as $L_x=80$, $k_{ymax}=2.4$, and M=9($k_{y0}=2.4/9$), and M=32($k_{y0}=2.4/32$); other parameters are the same as those in 3D case. The saturation amplitudes of the energy in these simulations are seen to be almost the same level. We find that (1) The QL effect, namely background modification does not play an essential role in determining the saturation level in the 3D simulations. (2) Aside from the QL effect, the 2D simulation gives an agreement to the 3D simulation. (3) The total mode number of $m\times n=9\times 12$ is enough in this simulations. In 3D cases, the stabilization due to QL effect is not essential for energy saturation. This is because the local pressure flattening does not occur in the 3D simulations. If the local flattening at some place occurs then it should induce the local pressure steeping in the neighborhood due to the constraint on the ion pressure at the calculation boundary. This does not happen in 3D simulations.

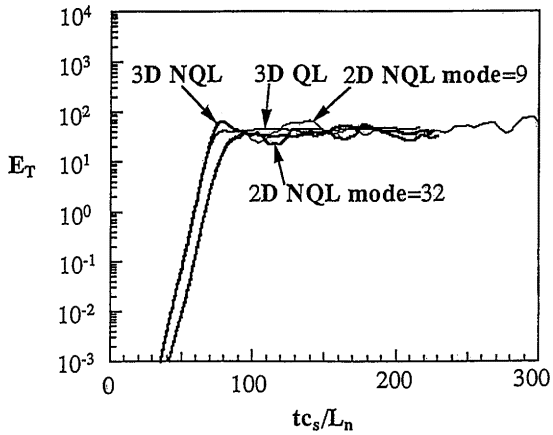

Fig. 13 The time evolution of energy in 3D QL and NQL calulation. Parameters are $S=0.1$, $K=3.0$, $\Gamma=2.0$, $\mu_{\perp c}=\chi_{\perp c}=0.1$, $\mu_{\parallel c}=\chi_{\parallel c}=1.0$. For 3D calculations, $L_x=80$ with 200 mesh, $k_{y0}=0.2$ with $M=10$, and $k_{z0}=0.267$ with $N=13$ are used ($k_y=mk_{y0}$, $0\leq m\leq 9$ and $k_z=nk_{z0}$, $-6\leq n\leq 6$). For comparison, 2D NQL simulations with $k_{ymax}=2.4$, $M=9$ and $M=32$ are also plotted ($k_{y0}=2.4/9$ and $k_{y0}=2.4/32$). Other parameters are the same as those in 3D simulations.

The agreement of the saturation level between the cases of 3D simulations and 2D NQL simulations give an insight in understanding the saturation mechanism for the slab η_i mode. In 2D cases, QL terms affect the saturation level; if we keep QL terms in 2D simulations, it brings to the one order smaller saturation amplitude. The influence of the profile modification appears strongly since modes are localized at single rational surface in 2D cases. The comparison study in Fig. 13 demonstrates that 2D NQL simulations are suitable for the parameter survey.

Figure 14 shows the power spectrum of the electrostatic potential $|\phi_{m/n}|^2$ in 3D NQL simulations at $t=104$. In this simulation, we use $L_x=80$ (400 mesh) and 255 modes. Other parameters are the same as those in Fig. 13. The mode rational surface is also shown at the bottom of this figure. The location of mode rational surface is represented by x_s. For comparison 2D NQL result at $t=200$

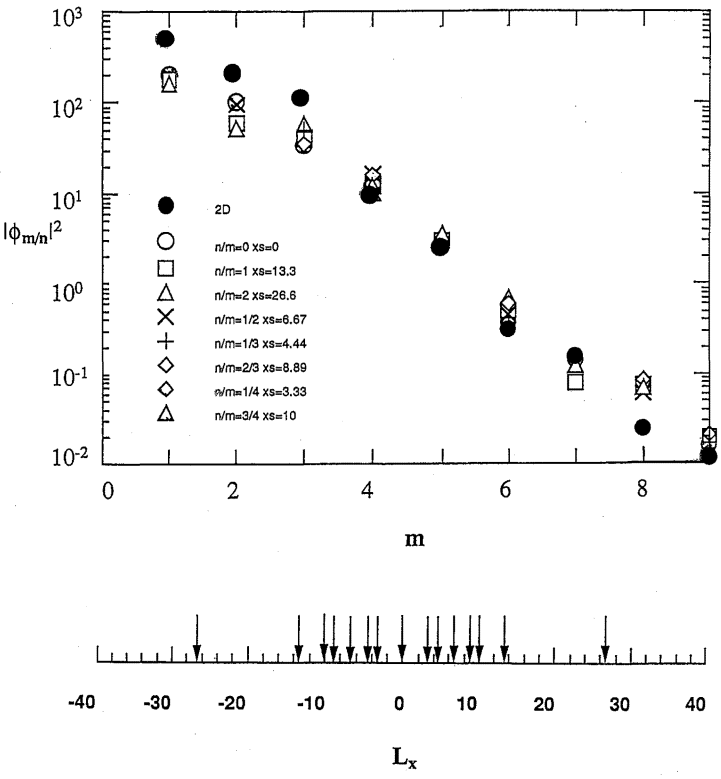

Fig. 14 The power spectrum of the potential in 3D NQL simulations. Parameters are $L_x = 80$ with 400 mesh and 255 modes. Other parameters are the same as those in Fig. 13. For comparison, 2D NQL simulation with $L_x = 40$, 200 mesh and $M = 9$ is also plotted.

is also shown. In this case, we use $L_x=40$ (200 mesh) and 9 modes. The shapes of the power spectrum are almost similar in 2D NQL and 3D NQL cases.

Next, we compare thermal diffusivity obtained from 2D NQL and 3D NQL simulations. Figure 15 shows the radial profiles of the thermal flux defined by Eq. (16) for the cases of linear calculation (top), 2D NQL (middle), and 3D NQL simulations (bottom), respectively. The thermal flux in the 2D simulation is localized around the rational surface. The estimate of the thermal diffusivity would depend on the system size if we use L_x for Δ_x in Eq. (11). For this reason, we use Δ_x as a normalization factor for 2D simulation.

Figure 16-(a) and 16-(b) shows the time evolutions of the ion thermal diffusivity evaluated from 2D NQL and 3D NQL simulations. The same parameters as in Fig. 13 are used for these calculations. The time average is done for the interval t=100-200. Transient peaks are observed in both cases. The thermal diffusivity reaches the level evaluated from the mixing length theory, at t=100 (i. e., the peak at t=100) in the case of 2D NQL simulation, and the peak at t=60 in the case of 3D one, then it settles down to the lower level. At this saturation state, the 2D NQL simulation gives the value of χ_i which is the similar value to the 3D NQL one (3D NQL/2D NQL$\sim$1.5).

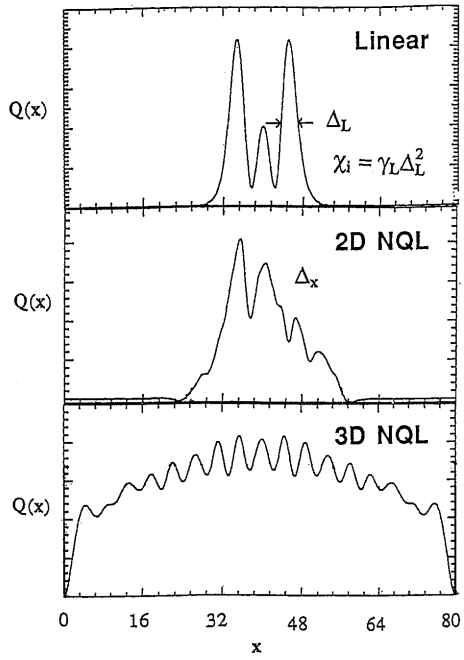

Fig. 15 The radial profile of the thermal flux for the linear (top), 2D NQL (middle), and 3D NQL (bottom) simulations.

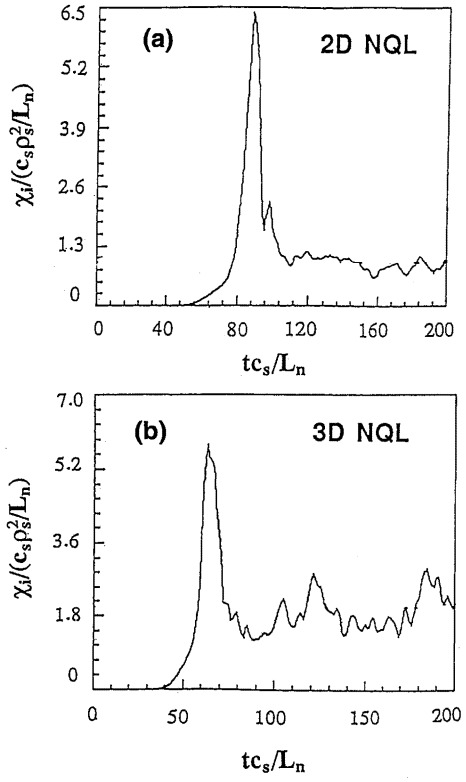

Fig. 16 (a) The time evolution of the ion thermal diffusivity evaluated from 2D NQL simulations. (b) The one from 3D NQL simulations. Parameters are the same as those in Fig. 13.

The dependencies of the thermal diffusivity on the parameter η_i and the shear S are summarized in Figure 17-(a) and 17-(b). The plasma parameters are the same as those in Fig. 13. The parameters for numerical simulation are $L_x=80$ with 300 mesh, $L_y=2\pi\times M/2.4$, with mode number M=64($k_{y0}=0.0375$ and $k_{ymax}=2.4$) for 2D NQL simulations. In the 3D simulations, we choose $L_x=80$ with 400 mesh, $L_y=10\pi$ with mode number M=9($k_{y0}=0.2$, $k_{ymax}=1.8$), and $L_z=7.5\pi$ with mode number N=15($k_{z0}=0.267$, $k_{ymax}=4.0$), total 9×30 mode. In these figures, the symbols of triangle and circle denote, the 3D NQL calculation and 2D NQL calculation, respectively. The symbol of square corresponds to the mixing-length-like estimate, $\chi_i=\gamma_L\Delta_L^2$, where γ_L is the linear growth rate and Δ_L is radial width of the linear eigenfunction. γ_L and Δ_L are obtained in the linear phase of the simulation ($t\leq40$). In this case of parameters above, the maximum growth rate is given at $k_y=0.6$. For 2D and 3D cases, we have plotted

the thermal diffusivity averaged over the time interval of t=150-300. From Fig. 17-(a) and 17-(b), we find general observations that the 2D NQL calculation gives a good approximation to 3D NQL calculation for η_i and S dependence in the range $10^{-2} \leq S \leq 1$ and $1 \leq \eta_i \leq 5$. Strictly speaking, the 2D case gives the slight stronger dependence on η_i and the slightly weaker dependence on S and the absolute value of 3D NQL is about 1.5 times larger that of 2D NQL. In section IV. E, we will discuss the reduced thermal diffusivity taking into account these results.

IV-D. Convergence Study

It is also important to study the influence of collisional diffusion. In above simulations, the artificial dissipation rates, $\chi_{\perp c}$, $\chi_{\parallel c}$, $\mu_{\perp c}$ and $\mu_{\parallel c}$ are set to be proper values. Namely, we use $\chi_{\parallel c} \sim 1$. This is because this viscosity acts as the parallel damping to the mode like as Landau damping. If we take too small

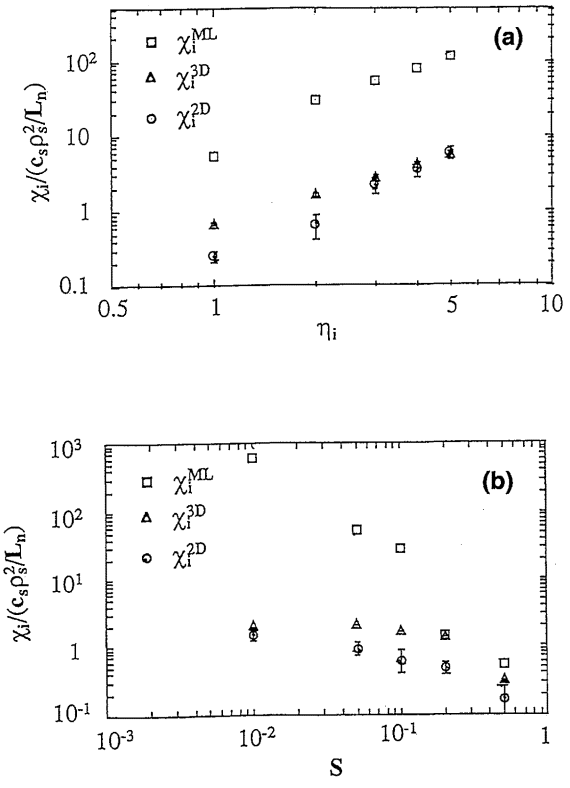

Fig. 17 (a) The dependence of the thermal diffusivity on η_i. (b) The dependence of the thermal diffusivity on S. Parameters are the same as those in Fig. 13.

value for $\chi_{\parallel c}$, the outgoing wave is not damped enough and reaches the simulation boundary. If is occurs then the reflection of the wave happens. This leads to the numerical instability. We also need the finite value of $\chi_{\perp c}$ for the energy in high wave number region to be damped. If the damping of the energy in high wave number region is not enough, the numerical reflection at $k_y = Mk_{y0}$ happens. This leads to no saturation and causes the numerical instability. In order to check the validity of the choice of these values, the $\chi_{\perp c}$ and $\chi_{\parallel c}$ dependencies on χ_i for 2D NQL simulations are examined and are shown in Figure 18-(a) and 18-(b). The parameters are the same as in Fig. 17. We assume $\chi_{\perp c} = \mu_{\perp c}$ for the $\chi_{\perp c}$ scan in Fig. 18-(a) and $\chi_{\parallel c} = \mu_{\parallel c}$ for the $\chi_{\parallel c}$ scan in Fig. 18-(b). It is easily seen that, for $\chi_{\perp c} < 0.1$ and $\chi_{\parallel c} < 1$, the thermal diffusivity is almost independent of $\chi_{\perp c}$ and $\chi_{\parallel c}$.

If they are too large, the turbulent transport considerably reduces. If they

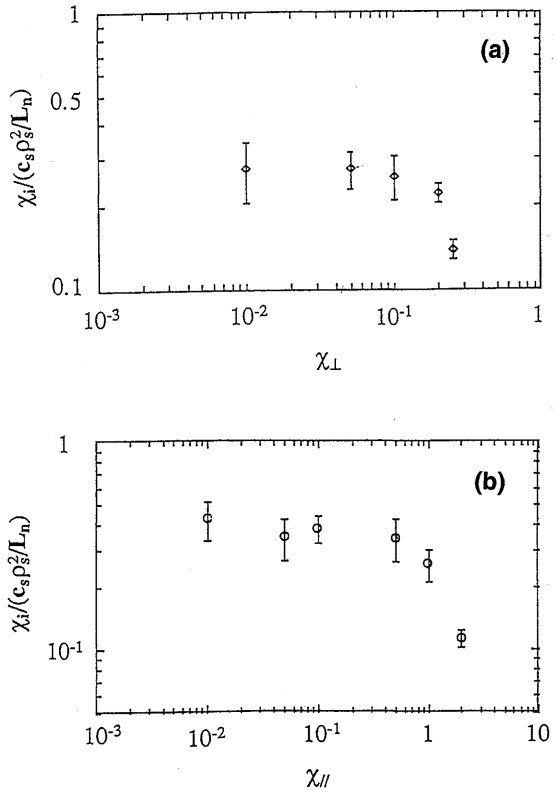

Fig. 18 (a) The dependence of the thermal diffusivity on $\chi_{\perp c}$. (b) The dependence of the thermal diffusivity on $\chi_{\parallel c}$. Parameters are the same as those in Fig. 13.

are too small, numerical instability occurs. Therefore we confirm the results in Fig. 17, where we take $\chi_{\perp c}=0.1$ and $\chi_{\parallel c}=1.0$, do not depend on these artificial dissipation describing subgrid scale dissipation and mode coupling. The convergence of the numerical simulation is thus confirmed.

IV-E. Deduced Thermal Diffusivity

Based on the 2D NQL results (Fig. 17), we obtain a fitting formula of the thermal conductivity as

$$\chi_i = C_0 \frac{\rho_s^2 c_s}{L_n}(\eta_i - \eta_{ic})^2 \exp(-3.38 S^{0.442}) \tag{19}$$

where C_0 is the numerical constant with order unity and $\eta_{ic} \sim 0.66$ for these parameters. Generally η_{ic} is the function of $\chi_{\perp c}$, $\chi_{\parallel c}$, $\mu_{\perp c}$, $\mu_{\parallel c}$, S, and Γ[5]. Using the amplitude expansion method [13, 14], Hamaguchi et al. [5]derived the formula $\chi_i \propto \eta - \eta_c$. Although we can fit the numerical results using this formula within the error bars, the relative error is larger than that of the formula with $(\eta - \eta_c)^2$ dependence. The formula like Eq.(19) suggests that the turbulence driven flux is enhanced if the driving force exceeds a critical value.

The discrepancy between the numerical simulation and the mixing-length estimate lies on the shear dependence. This is illustrated by seeing the analytic estimation of the formula $\gamma_L/k_\perp^2$. If one employs the analytic estimate for γ_L and $k_\perp$, which are given in connection with Eq.(17), one finds $\chi_i \propto K^{3/2} S$ for $KS \ll 1$ and $\chi_i \propto K^{3/4} S^{1/4}$ for $KS \gg 1$[15].This shear dependence (i. e., χ_i increases if S increases) has clearly the opposite tendency compared with the numerical result. This is partly from the inaccuracy of the analytic estimate of γ_L and $k_\perp$ as pointed out in Ref.[5]. If one uses the numerical result of γ_L and Δ_L, χ_L^{ML} becomes a decreasing function of S. However, it still overestimates χ_i particularly in the low shear region.

The absolute value of the thermal diffusivity given by the mixing-length-like estimate, $\chi_i = \gamma_L \Delta_L^2$ is one order higher than others, while it's dependence on η_i is similar to those of nonlinear simulations. The difference of the absolute values between the numerical result and the mixing-length-like estimate in Fig. 17-(b) is also attributed to the shear dependence. For high shear limit, the mixing-length-like estimate gives the thermal diffusivity of the order which is comparable to those of 2D and 3D calculations if γ_L and Δ_L correctly chosen. But in the low shear limit, the difference is large. In the weak shear limit, the linear mode structure becomes broad since high l mode becomes more unstable so that the value $\gamma_L \Delta_L^2$ is estimated to be larger. From the view point of the shear dependence and the absolute value, the simple mixing-length estimate using γ_L and Δ_L is not appropriate for the η_i mode.

V. Discussion and Conclusion

A systematic comparison of the 2D and 3D simulations for the slab η_i mode

was developed: 3D QL 3D NQL, 2D QL and 2D NQL models were investigated. Based on this systematic study, we find that (1) the background modification of the temperature profile is not important in the 3D simulation, that (2) the strong stabilization in the 2D QL model by the back ground profile modification is an overestimate, and that (3) the 2D NQL simulation gives a similar parameter dependence as well as the absolute value for the thermal diffusivity in comparison with the 3D simulation. It is concluded that the 2D NQL simulation allows a rapid and dependable nonlinear simulation of the η_i mode. This will provide the basis of the future parameter survey through the nonlinear simulation. The mixing-length-(like) estimate was found to be inaccurate, from the view point of the absolute value and the shear dependence. This also stimulates the future nonlinear study by use of the 2D NQL model, in order to clarify the detailed mechanism of the saturation of the turbulence.

For the application, the comparison of 2D NQL simulation of η_i mode turbulence with experimental results were performed in Ref.[10]. We found that the absolute value of the thermal diffusivity obtained from the 2D NQL simulation is the same order as that evaluated from JT-60 experimental data, although it's radial dependence is different from the experimental one. The important point is that the mixing-length estimation only gives us the functional dependence of thermal diffusivity (although in the η_i mode case, the shear dependence is incorrect) but not it's absolute value. Therefore it is possible to analyze experimental data more quantitatively by using simulations.

These findings will be the basis for the future investigations in which Eqs. (1) and (2) will be solved without simplifications.

Acknowledgments

A major part of this work has been performed when the author stayed in Japan Atomic Energy Research Institute. The author gratefully acknowledges Dr. M. Azumi for fruitful discussions and support to accomplish this work. Without this support, this work would not be completed. Also he acknowledges Profs. S.-I. Itoh, K. Itoh, A. Fukuyama, M. Wakatani, W. Horton for collaborations and useful discussions, Dr. H. Shirai for computational support. This work is partly supported by the Grant-in-Aid for Scientific Research of Ministry of Education Japan, by the collaboration program between universities and Japan Atomic Energy Research Institute on fusion and by collaboration program of Advanced Fusion Research Center of Kyushu University.

References

1) P. C. Liewer, Nucl. Fusion **25** (1985) 543.
2) B. B. Kadomtsev and V. I. Petviashvili, Sov. Phys. JETP **17** (1963) 403.
3) W. Horton, Phys. Rep. **192 (1-3)** (1990) 1.
4) W. Horton, R. D. Estes, and D. Biskamp, Plasma Physics **22** (1980) 663.
5) S. Hamaguchi and W. Horton, Phys. Fluids **B2** (1990) 1833.

6) R. E. Waltz, Phys. Fluids **29** (1986) 3684.
7) AIP Conference Proceedings 284, U. S.-Japan Workshop on Ion Temperature Gradient-Driven Turbulent Transport, Austin, TX, 1993, edited by W. Horton, M. Wakatani, and A. Wooton (American Institute of Physics, New York, 1993).
8) M. Yagi, K. Itoh, S.-I. Itoh, A. Fukuyama, M. Azumi, Phys. Plasmas **2** (1995) 4140.
9) B. Coppi, M. N. Rosenbulth, and R. Z. Sagdeev, Phys. Fluids **10** (1967) 582.
10) M. Yagi and M. Azumi, AIP Conference Proceedings 284, U. S.-Japn Workshop on Ion Temperature Gradient-Driven Turbulent Transport, Austin, TX, 1993, edited by W. Horton, M. Wakatani, and A. Wooton (American Institute of Physics, New York, 1993), p. 87.
11) S. Chandrasekhar, in Hydrodynamic and Hydromagnetic Stability (Dover, New York, 1961), p. 16.
12) P. H. Rutherford, Phys. Fluids **16** (1973) 1903.
13) S. Hamaguchi, Phys. Fluids **B1** (1989) 1416.
14) D. D. Joseph, Stability of Fluid Motion (Springer, New York, 1976), Vols. I and II.
15) J. W. Connor, Nucl. Fusion **26** (1986) 193.

(Received May 27, 1996)